Satellite remote sensing of dust aerosol indirect effects on ice cloud formation

Steve Szu-Cheng Ou,[1,*] Kuo-Nan Liou,[1] Xingjuan Wang,[1] Richard Hansell,[1,2] Randy Lefevre,[3] and Stephen Cocks[3]

[1]University of California, Los Angeles, California 90095, USA

[2]NASA/Goddard Space Flight Center, Greenbelt, Maryland 20771, USA

[3]Airborne Laser System Program Office, Kirtland AFB, New Mexico 87117, USA

*Corresponding author: ssou@atmos.ucla.edu

Received 15 July 2008; revised 3 December 2008; accepted 7 December 2008; posted 8 December 2008 (Doc. ID 98853); published 16 January 2009

We undertook a new approach to investigate the aerosol indirect effect of the first kind on ice cloud formation by using available data products from the Moderate-Resolution Imaging Spectrometer (MODIS) and obtained physical understanding about the interaction between aerosols and ice clouds. Our analysis focused on the examination of the variability in the correlation between ice cloud parameters (optical depth, effective particle size, cloud water path, and cloud particle number concentration) and aerosol optical depth and number concentration that were inferred from available satellite cloud and aerosol data products. Correlation results for a number of selected scenes containing dust and ice clouds are presented, and dust aerosol indirect effects on ice clouds are directly demonstrated from satellite observations.

OCIS codes: 010.1650, 010.1110.

1. Introduction

The global mean burden of aerosols has been constantly increasing from preindustrial times to the present day. Major species of atmospheric aerosols include mineral dust particles lifted from desert surfaces by dust storms and transported across continents and oceans by atmospheric general circulation, organic suspensions and inorganic particles injected by biomass burning and wild fires, and haze particles associated with urban air pollution. Moreover, due to the substantial increase in air traffic in recent years, soot particles composed mainly of black carbon (BC), along with sulfur compounds and water vapor, have infiltrated the upper troposphere, causing increased frequency in the occurrence of contrails and contrail-induced cirrus clouds [1–4].

By means of absorption and scattering processes, aerosols affect atmospheric radiative transfer through their direct interaction with solar radiation. Aerosols also affect atmospheric radiative and climate forcings indirectly through their interaction with clouds by modifying cloud optical properties and precipitation efficiency. The direct radiative effect of aerosols is much smaller than that of clouds. However, their indirect effects on cloud formation and coupled radiative effects are critically important in conjunction with energy balance and hydrological cycle of the Earth–atmosphere system [5]. To effectively quantify the radiative and climatic effect of ice clouds induced by the presence of aerosols, a term referred to as the radiative forcing, defined as the difference between shortwave and longwave radiative fluxes under cloudy and cloud-free conditions, has been used to understand and quantify the aerosol indirect effect. Significant uncertainties exist in current climate models and observations in the assessment of radiative forcing of the aerosol-induced ice cloud formation [6].

Lohmann and Feichter [7] provided a comprehensive review of the current status of research in global

0003-6935/09/030633-10$15.00/0

aerosol indirect effects. The aerosol indirect effect of the first kind is now referred to as the "Twomey effect" [8], an effect involving increases in solar cloud albedo due to decreases in cloud particle sizes caused by additional aerosols serving as cloud condensation nuclei (CCN) and ice nuclei (IN). Other types of indirect effects have also been identified and are referred to as the aerosol indirect effect of the second kind, including the effect on cloud lifetime and precipitation efficiency caused by additional smaller cloud particles [9,10] and the solar absorption effect of soot particles related to decreases in the precipitation efficiency [11,12]. The Twomey effect on low-level stratiform water clouds has been distinctly observed by satellite radiometers. The most notable example is the observation of perturbed marine stratus cloud decks that hover over ship tracks off the coast of California [13]. At this point, the aerosol indirect effect of the first kind on water clouds has been well studied [14]. However, investigation of this effect in association with ice clouds has been extremely limited, and large uncertainties exist for its quantification.

The formation of ice crystals in high-level clouds involves the homogeneous freezing of solution droplets formed on soluble CCN at temperatures below −37°, as well as the heterogeneous freezing processes involving insoluble or partially soluble IN. The leading IN candidates are mineral dust and BC [15]. In particular, dust particles generally originate from arid desert surfaces and can be transported thousands of miles away before they eventually settle back onto the surface again [16–18]. Dust particles can also be lifted upward into the middle and upper troposphere, where they can interact with high-level clouds and modify their microphysical and radiative properties [19]. Also note that elevated dust particles can serve as IN via the deposition nucleation. Based on laboratory studies, surrogates for mineral dust particles proved to be strong contributors to heterogeneous IN populations, and it has been found that heterogeneous freezing rates increase with dust particle size under the same thermodynamic conditions [20].

We have developed an approach to investigate the dust aerosol indirect effect involving ice clouds through analysis of the data gathered from satellite remote sensing and have provided a better understanding of the cause-and-effect relationship between dust and ice cloud formation. Section 2 describes the processing and analysis of satellite data, followed by the presentation of correlation results between ice cloud and dust aerosol properties in Section 3. Concluding remarks are given in Section 4.

2. Analysis of Satellite Data

The analysis of satellite data begins with the identification of Moderate-Resolution Imaging Spectrometer (MODIS) scenes and dust/ice-cloud areas. For a selected scene, we first search for regions that clearly display the simultaneous presence of aerosols and ice clouds over both water and land surfaces. Heavy aerosol areas over dark surfaces normally appear in hazy light-yellow-brownish or light-blue color. Aerosols are identified as clear pixels based on the MODIS cloud mask along with aerosol optical depths available from the existing database, and aerosols originated from dust-prone regions were determined by the MODIS aerosol algorithm to be primarily consisting of mineral dust [21]. In addition, examination of the MODIS red-green-blue images indicates that ice cloud areas are normally characterized by white-colored hairy cloudy pattern. Ice clouds are identified by the MODIS cloud and cloud-phase masks when their optical depths are larger than zero.

To determine the ice crystal number concentration (N_i), we first define the ice water content (IWC) as follows:

$$\mathrm{IWC} = \rho_i \int v_i(L) n_i(L) \mathrm{d}L, \tag{1}$$

where L is the ice crystal maximum dimension, $v_i(L)$ is the single ice crystal volume as a function of L, n_i is the ice crystal size distribution, and ρ_i is the ice crystal mass density. We can define a characteristic mean particle volume, $\bar{v}_i$, in the form

$$\bar{v}_i = \frac{\int v_i n_i(L) \mathrm{d}L}{\int n_i(L) \mathrm{d}L} = \frac{\int v_i n_i(L) \mathrm{d}L}{N_i}. \tag{2}$$

To get N_i, we first use the MODIS-retrieved ice cloud optical depth, τ_c, and mean effective particle radius, r_e, to determine IWC based on the parameterization of these three variables as follows [22]:

$$\mathrm{IWC} = \tau_c / [(a + b/r_e)\Delta z_c], \tag{3}$$

where $a = -6.656 \times 10^{-3}\,\mathrm{m}^2/\mathrm{gm}$ and $b = 3.686\,\mathrm{m}^2 - \mu\mathrm{m}/\mathrm{gm}$, and Δz_c is the cloud geometric thickness. Collocated lidar dataset, if available, can be used to determine Δz_c. However, we do not have lidar data for all the selected cases, and we have prescribed ice cloud thickness using climatological values [23]. Subsequently, we obtain $\bar{v}_i$ from a relationship between ice particle size distribution and cloud temperature developed from statistical analysis of aircraft *in situ* microphysical observations [24]. Since the mean ice crystal effective size increases with cloud temperature, we expect that $\bar{v}_i$ also increases with cloud temperature.

Likewise, the aerosol number concentration (N_a) can be determined from a similar procedure. The aerosol mass concentration (AMC) can be expressed as follows:

$$\mathrm{AMC} = \rho_a \int v_a(r) n_a(r) \mathrm{d}r, \tag{4}$$

where r is the aerosol particle radius, $v_a(r)$ is the aerosol volume as a function of r, n_a is the aerosol size

distribution, and ρ_a is the aerosol mass density. We can define a mean aerosol particle volume such that

$$\bar{v}_a = \frac{\int v_a n_a(r)\mathrm{d}r}{\int n_a(r)\mathrm{d}r} = \frac{\int v_a n_a(r)\mathrm{d}r}{N_a} = \frac{\mathrm{AMC}}{\rho_a N_a}. \quad (5)$$

The value of $\bar{v}_a$ and ρ_a can be estimated based on *in situ* or laboratory observations or an aerosol composition and a size distribution assumed *a priori* [25]. To get N_a from Eq. (5), we use the MODIS-retrieved aerosol optical depth, τ_a, together with a prescribed mean effective particle size, r_a, defined by

$$r_a = \int \frac{r^3 n_a(r)\mathrm{d}r}{r^2 n_a(r)\mathrm{d}r}, \qquad \tau_a = 2\pi\Delta z_a \int r^2 n_a(r)\mathrm{d}r,$$

where Δz_a is the aerosol layer thickness, which can be determined based on an available collocated lidar dataset. If a collocated lidar dataset is not available, instead of prescribing Δz_a, a vertically mean extinction coefficient ($\beta_{\mathrm{ext}} = \tau_a/\Delta z_a$) can be extracted from tabulated climatological values for dust-like aerosols [26]. Assuming that aerosols are spherical ($v_a = \frac{4}{3}\pi r^3$), we obtain from Eq. (4) the following relationship:

$$\mathrm{AMC} = \frac{2}{3}\rho_a r_a \tau_a/\Delta z_a. \quad (6)$$

Equation (6) is different from Eq. (3) in form, because Eq. (3) was derived based on the assumption that ice clouds are composed of nonspherical randomly oriented ice crystals [22].

Both the estimated $\bar{v}_i$ and $\bar{v}_a$ can be subject to uncertainties whose effects on correlation analysis require detailed sensitivity studies based on *in situ* measured ice crystal and aerosol size distributions (also subject to uncertainties) that are collocated with satellite observations, a subject requiring further investigations. Nevertheless, we have demonstrated the validity of derived cloud and aerosol properties by comparing with *in situ* measurements (see Section 3 below).

To correlate ice and aerosol properties, we have divided the identified aerosol/ice-cloud domain into a number of multipixel subgrids. Because the MODIS cloud mask program identifies a pixel either as clear/aerosol or cloud, and because the current MODIS cloud and aerosol algorithms cannot simultaneously detect/retrieve aerosol and cloud parameters for a single pixel, we have performed the correlation analysis using the average aerosol and cloud properties within each subgrid that contains both ice cloud and aerosol pixels. Aerosol/cloud optical depth and particle size have been routinely retrieved by MODIS algorithms. For visible and near-IR window bands used in the MODIS cloud retrieval program, effects of water vapor absorption/emission on reflectance/radiance are minimal in relation to the quantification of aerosols in the vicinity of clouds. The horizontal variation of satellite-inferred cloud properties within these relatively small subgrids would be primarily caused by microphysical processes involving aerosol–cloud interactions, since the spatial and time scales associated with the variability of aerosols (on the order of microns and seconds) are substantially smaller than those associated with meteorological drivers (on the order of kilometers and hours). Moreover, because of the very high spatial resolution of MODIS data ($\sim$0.25–1 km^2) and the excellent and effective capability of the MODIS cloud mask program to detect cloud pixels, it is anticipated that effects of cloud contamination on the inference of the aerosol field would be minimal [27].

We have also carefully taken into account the complexity of retrieving aerosol products in the presence of thin cirrus clouds. Since the MODIS cloud mask program contains state-of-art operating algorithms that were developed and implemented specifically for the effective detection of thin cirrus clouds, the problem of cirrus contamination in aerosol products has been minimized. In our study, we have ensured that only the aerosol property products for pixels flagged by the MODIS cloud mask program as "confidently clear" were extracted for analysis. These confidently clear pixels have been identified through a series of stringent threshold tests, including the 1.38 μm band reflectance test, which is particularly efficient in identifying high thin cirrus clouds [28]. Thus, it is anticipated that the probability of a detected aerosol pixel being contaminated by cirrus is extremely small. On the other hand, effects of contamination by aerosols imbedded in ice cloud pixels on the retrieved cloud optical depth and effective particle size are expected to be negligible, because the contribution of cloud reflection typically dominates the total reflectance due to the relatively small aerosol optical depth. Thin cirrus cloud pixels with $\tau_c < 1$ are not included in the analysis.

We searched for statistically meaningful correlations between ice cloud and aerosol number concentrations based on the criterion that the magnitude of the correlation coefficient is larger than a threshold value. Subsequently, a parameterized relationship between them is developed using a least-square fitting technique.

3. Application to the MODIS Scenes Containing Dust and Ice Clouds

A. Dust Aerosol Indirect Effect on Ice Clouds Formed on Top of a Transported Dust Layer

We examined MODIS data covering the regions of frequent dust outbreaks in East Asia, the Middle East, and Western Africa, and areas associated with long-range dust transportation such as the equatorial tropical Atlantic Ocean. Based on visual inspection and cloud mask results, we have chosen a number of interesting MODIS dust scenes to study the Twomey effect on ice clouds. These scenes contain both dust/aerosols and clouds. Cloud and aerosol

optical depths and cloud particle sizes inferred from MODIS for selected domains were analyzed from which the parameters IWP, N_i, N_w, and N_a were subsequently derived. The unified ice crystal light scattering theory [29,30] for all ice crystal sizes and shapes was adopted in the retrieval of ice cloud optical properties. This unified theory is a unification of an improved geometric ray-tracing/Monte Carlo method for size parameters larger than about 15 and a finite-difference time domain method for size parameters less than 15. Based on MODIS cloud optical properties and aerosol product Algorithm Theoretical Basis Documents [31,21], uncertainties in retrieved τ_c and r_e are less than 10% and 3 μm, respectively, while estimated errors in retrieved τ_a are nearly zero for $\tau_a < 1$ and less than 10% for $1 \le \tau_a \le 5$. These MODIS cloud and aerosol products were obtained on the basis of the independent-pixel assumption. The effect of three-dimensional radiative transfer was not included in the retrieval algorithm, a subject that requires further investigation and is beyond the scope of the present study. As mentioned above, the selected domain was divided into a number of subgrids to develop statistical correlations between the subgrid mean cirrus cloud and dust parameters and to investigate the variability and physical significance of these correlations.

In the following, we present a case of dust aerosol indirect effect on glaciated ice clouds. We based our investigation on a prominent case of 29 July 2002, detected by pulse detecting lidar (PDL) during the Cirrus Regional Study of Tropical Anvil and Cirrus Layers—Florida Area Cirrus Experiment (CRYSTAL-FACE) in the southwest coast of Florida, a campaign to study subtropical high-level cirrus and aerosols. The observations were initially designed to study cirrus layers, but at the same time captured a depolarizing aerosol layer extending from the top of the boundary layer (~1.7 km above mean sea level) to ~5.5 km. Figure 1 as adopted from Ref. [19] provides the height-versus-time displays of the PDL linear depolarization ratio (δ) and relative returned power from the Ochopee field site of the CRYSTAL–FACE program in the morning. The altocumulus at far right containing supercooled spherical droplets produces near-zero depolarization at the liquid cloud base with a gradual increase aloft due to multiple scattering effects in the optically denser portions of the cloud. As the layer height decreased, glaciation occurred at 1516 UTC and displayed depolarization δ of 0.3–0.4. This glaciation took place close to the top of the dust layer. The average temperatures measured by the University of North Dakota (UND) Citation aircraft during takeoff and landing at the altocumulus cloud base and top heights are relatively warm with temperatures at −5.2 and −8.8° C, respectively.

In conjunction with this case, we analyzed the MODIS/Aqua data collocated with the PDL ice cloud detection on 29 July 2002. Figures 2(a)–2(d) display ice cloud optical depth (τ_c), mean effective particle

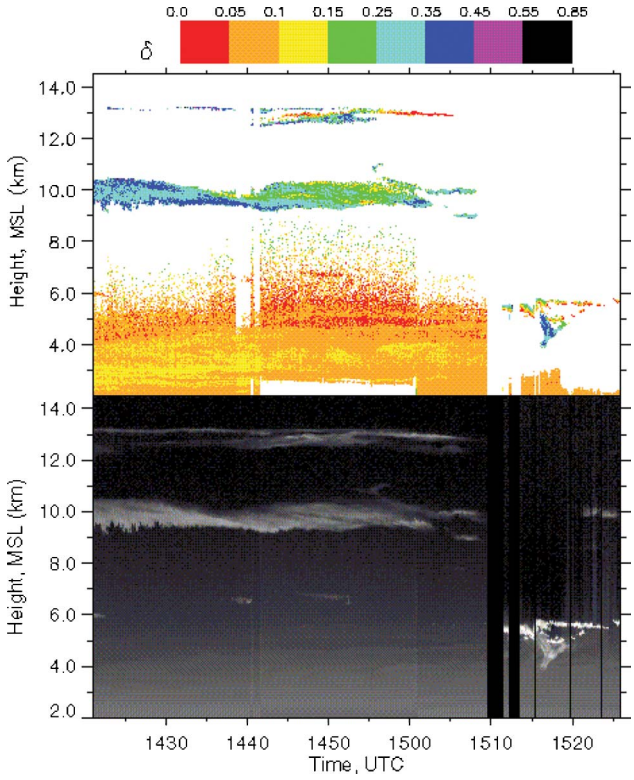

Fig. 1. (Color online) PDL linear depolarization ratio (see color scale at top) and relative returned power (in a logarithmic gray scale) height-versus-time displays on the morning of 29 July 2002, from the Ochopee field site of the CRYSTAL—FACE program. Depicted are strongly depolarizing ($\delta = 0.2$ to 0.4) upper tropospheric cirrus clouds, aerosols ($\delta = 0.10$ to 0.15) extending up to ~5.5 km, and at far right a supercooled liquid altocumulus cloud ($\delta = 0$ at cloud base). Note the temporary glaciation of this cloud as it descended into the top of the dust layer.

size (r_e), cloud temperature (T_c), and aerosol optical depth (τ_z). For the identified ice cloud region collocated with the lidar site denoted by the orange circle, τ_c varies between 0 and 20 with a majority of pixels showing values less than 10, while r_e ranges between 0 and 60 μm with a majority of pixels showing values between 10 and 20 μm. T_c is shown to be between 200 and 260 K with a distribution peak near 260 K, consistent with the lidar measured cloud-top height at 5.5 km. Humidity and temperature soundings during the UND Citation takeoff and landing also reveal a distinct moist layer (RH ~ 100%) between 4 and 6 km with a temperature near the top of this moist layer of 260 K, which matches the majority of MODIS cloud-top temperature values. The aerosol optical depth τ_a varies between 0.2 and 0.7 with a distribution peak at 0.45.

In Figs. 2(e)–2(h), we display a number of correlation studies involving τ_c versus τ_a, r_e versus τ_a, IWP versus τ_a, and N_i versus N_a. The cloud IWP, ranging from 0 to 140 g m^{-2}, was derived from τ_c and r_e. The average cloud geometrical thickness is about 1.5 km based on lidar measurements [19], leading to a range of IWC from 0 to 0.093 g m^{-3}. Note that the maximum IWC is close to the climatological value of 0.1 g m^{-3}

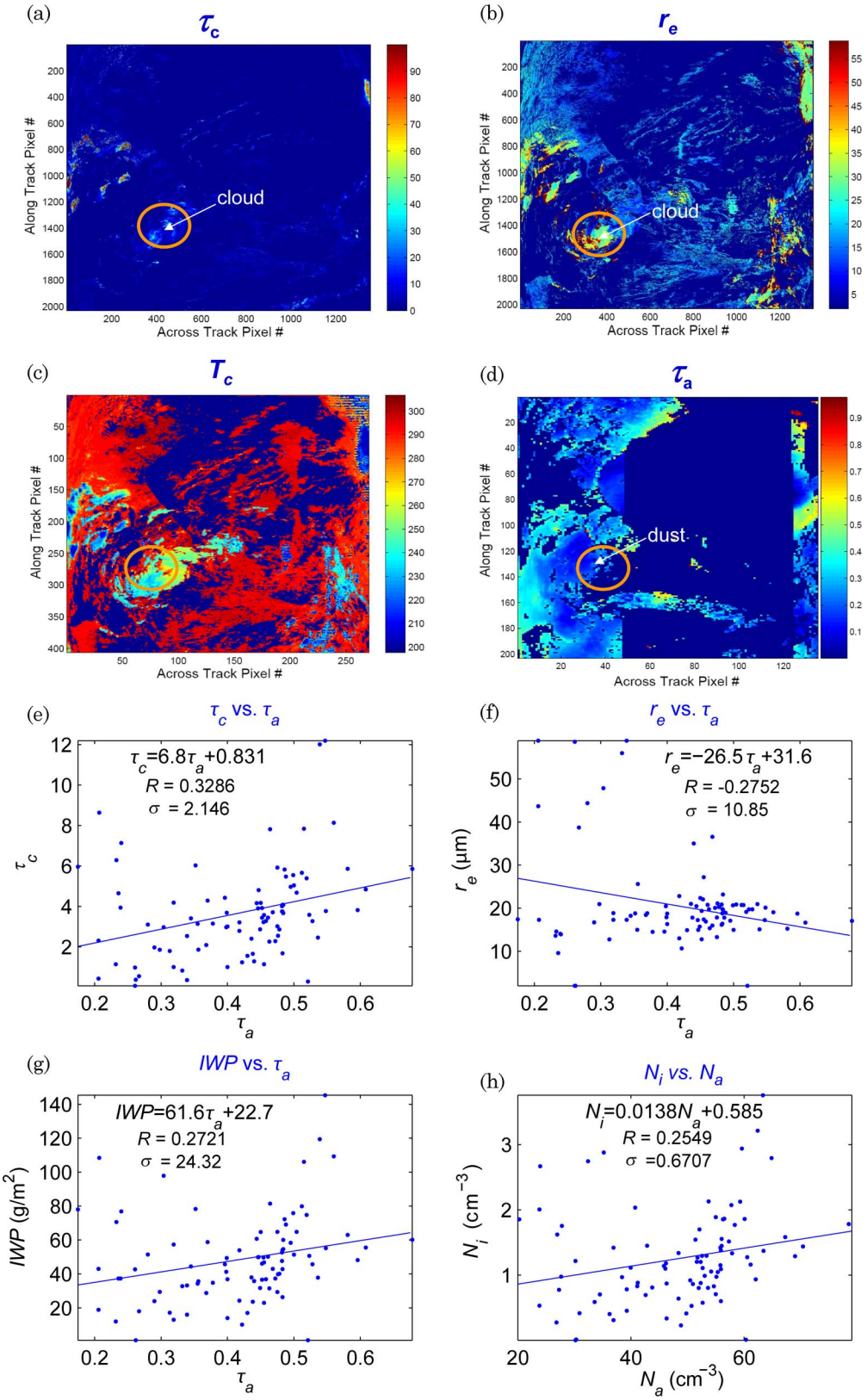

Fig. 2. (Color online) MODIS retrieval products for 29 July 29 2002 at 1600 UTC over southern Florida: (a) cloud optical depth (τ_c), (b) effective particle size (r_e), (c) cloud-top temperature (T_c), and (d) aerosol optical depth (τ_a). The orange-circled areas display aerosol and cloudy regions that correspond to the glaciated altocumulus observed by the PDL. The selected domain was divided into a number of subgrids, and statistical correlations between the subgrid mean cirrus cloud and dust parameters were developed and are shown in (e)–(h): (e) τ_c versus τ_a, (f) r_e versus τ_a (g) *IWP* versus τ_a, and (h) N_i versus N_a. The straight lines denote linear fittings of the data points, with the fitting equation, coefficient of correlation (R) and standard deviation (σ) given at the top of each frame.

shown in Liou (2002, Fig. 8.15) [22]. The number concentrations N_i and N_a vary between 0 and 4 cm^{-3} and between 20 and 80 cm^{-3}, respectively. The former number compares reasonably well with *in situ* measurements obtained from the continuous flow diffusion chamber (CFDC) onboard the UND Citation II [32], while the latter number compares closely to the Miami aerosol mass concentration measurements during the CRYSTAL-FACE campaign, 28–29 July 2002 [19]. Within the dust layer between 1 and 4 km, the CFDC measurements show that the number density of IN was between 0.01 and 1 cm^{-3} and N_a varied between 1 and 100 cm^{-3}. The Miami aerosol measurement record shows three episodes of the mineral dust burst in July. The maximum mass concentration of mineral dust ($\sim$40 $\mu g\, m^{-3}$) occurred during the 28–29 July period. Given that the dust density is about 2 $g\, cm^{-3}$ and that the mean dust radius is 0.5 μm, this maximum mass concentration corresponds to a number concentration of $\sim$40 cm^{-3}. The range of inferred N_a is of the same order of magnitude as this observed value.

Based on a linear fitting of the data points, both τ_c and IWP generally increase with τ_a, whereas cloud effective particle radius r_e decreases with increasing τ_a. The trend of r_e versus τ_a illustrates that there is a correlation between these two parameters, consistent with the hypothesis of the Twomey effect involving dust and ice clouds. Also note that the cloud number concentration N_i increases when dust number concentration N_a increases. This can be physically interpreted in terms of an aerosol-induced cloud phase change. With ample moisture supply, as evidenced by the high relative humidity in the cloud layer, liquid cloud droplets were first formed on CCN. As these cloud droplets descend into the dust layer, dust particles, serving as effective IN, trigger glaciation. Increasing aerosol optical depth would provide more IN, leading to smaller ice crystal sizes due to the competition for moisture.

Figures 2(e)–2(h) also include the coefficients of correlation (R) and the standard deviations (σ). However, both R and σ can only give an indication of the extent of cloud inhomogeneity, and cannot be used to quantify the Twomey effect. For example, Fig. 2(f) shows some spread of data points ($0 < \tau_c < 10$ for $\tau_a < 0.4$) caused by cloud inhomogeneity, as reflected by the relatively small $R(= -0.26)$ and large $\sigma(= 10.8\,\mu m)$. The Twomey effect can be statistically quantified based on the slope of best-fit straight lines in the correlation study. Figures 2(e)–2(h) show that the slope values of $\Delta\tau_c/\Delta\tau_a$, $\Delta r_e/\Delta\tau_a$, $\Delta IWP/\Delta\tau_a$, and $\Delta N_i/\Delta N_a$ are 6.8, $-26.5\,\mu m$, 61.56 $g\, m^{-2}$, and 0.014, respectively. These values are indicative of the sensitivity of ice cloud properties to variation in aerosol properties and are dependent on such factors as relative humidity and ice cloud and dust aerosol optical properties that vary with location and time. Feingold *et al.* (2003) [33] quantified the aerosol indirect effect (AIE) for water clouds in terms of the following index:

$$AIE = -(d \ln r_e)/(d \ln \alpha), \tag{7}$$

where α is the aerosol extinction coefficient. The AIE range for water clouds is found to be between 0 and 0.33. For the present ice cloud, we assume that $d \ln \alpha = d \ln \tau_a$, which is valid for a constant geometrical thickness of the dust layer.

Based on the mean retrieved r_e and τ_a of 16.03 μm and 0.403, respectively, and the slope $\Delta r_e/\Delta\tau_a = -26.5\,\mu m$, the estimated AIE is 0.67, about twice as large as the maximum value proposed by Feingold *et al.* It must be noted that in deriving the maximum value of AIE (0.33), Feingold *et al.* assumed that cloud liquid water content is constant and that cloud droplets are spherical. In the present study, IWC is not constant, but increases with τ_a, as shown in Fig. 2(g). Using the AIE index, it appears that the present case illustrates a significant dust indirect effect on ice cloud formation that is more prominent than typical aerosol indirect effects for water clouds.

B. Dust Aerosol Indirect Effect on Cirrus Clouds with Different Dust Loadings

In addition to the lidar depolarization technique, we can also identify aerosol indirect effect by comparison of a number of cirrus cloudy regions with different dust loadings. To the best of our physical understanding, cirrus clouds over a heavier dust area (with many of dust particles serving as potential IN) would likely be affected more than those over a lighter dust region. With this understanding, we performed statistical analysis involving two cases that occurred in Western Africa and Korea. For each case, we compared the mean effective cloud particle sizes for cirrus in proximity with different dust loadings. For the Korean case, we also carried out statistical analysis to evaluate the dust Twomey effect for different cirrus cloudy regions.

Figure 3(a) shows a Terra/MODIS scene for the date 23 September 2006 at 1210 UTC over the Eastern Tropical Atlantic Ocean and Western Africa. Near the southwest corner, we see an area of the transported dust layer characterized by a light-yellowish background with clouds imbedded in it. We selected regions A and B, which contain cirrus clouds on top of a heavier and a lighter dust layer, respectively. Within these regions, the brightness temperature differences between 11 and 12 μm bands (BTD11-12) and between 8.55 and 11 μm bands (BTD8-11) vary between 0 and 4 K and between 0 and 5 K, respectively. These positive values of BTD11-12 and BTD8-11 indicate semitransparent to opaque cirrus clouds. The 1.38 μm band reflectance also displays nonzero values for both regions, further confirming that the area contains cirrus clouds. In addition, MODIS cloud mask shows that the area is masked by cloudiness, and its cloud-phase mask indicates that parts of the cloudiness within both regions are ice clouds. Table 1 provides a list of parameters and their mean values for domains A and B. Low T_c values for both domains further confirm the

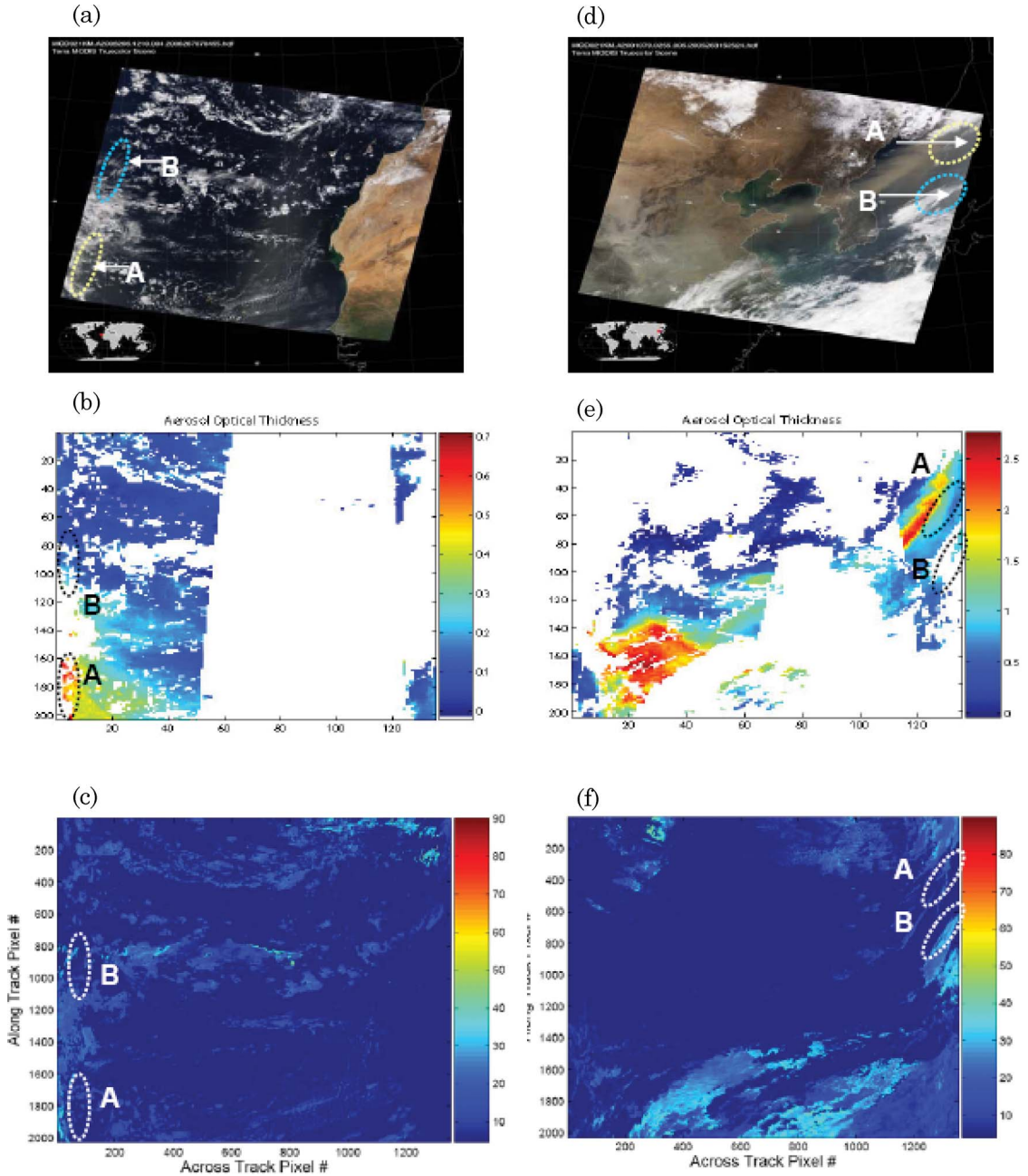

Fig. 3. (Color online) MODIS scenes with simultaneous presence of cirrus cloud and dust layers. Images for MODIS overpass on 23 September 2006 at 1210 UTC over western Africa: (a) RGB, (b) aerosol optical depth, and (c) cloud effective particle size. Images for MODIS overpass on 20 March 2001 at 1210 UTC over Korea: (d) RGB, (e) aerosol optical depth, and (f) cloud effective particle size.

existence of ice clouds. For domain A, τ_a varies between 0.42 and 0.6 [Fig. 3(b)] with a mean value of 0.49, while r_e varies between 0 and 70 μm, with a mean value of 29.1 μm [Fig. 3(c)]. For domain B, we determine τ_a in the range 0.12–0.25 [Fig. 3(b)] with a mean value of 0.16, and r_e in the range 0–90 μm [Fig. 3(c)], with a mean value of 32.4 μm. It is evident that for domain A, the dust optical depth is larger, but at the same time the cloud particle size is smaller, consistent with the Twomey effect for aerosol–water cloud interactions.

Table 1. Parameter Ranges and Their Mean Values for Domains A and B of the MODIS Scene for 23 September 2006 at 1210 UTC over Eastern Tropical Atlantic Ocean and Western Africa

	Parameter Range (mean value)			
Region	τ_c	r_e (μm)	$T_c(K)$	τ_a
A	0–30 (3.25)	0–70(29.1)	200–260(220)	0.42–0.6(0.49)
B	0–10(1.76)	0–90(32.4)	200–270(220)	0.12–0.25(0.16)

Figure 3(d) shows the other Terra/MODIS scene over Korea for the date 20 March 2001 at 0255 UTC. A distinctive yellowish-brown dust band extended from the tip of China's Shangdong Peninsula, across the Korean Peninsula to the Eastern Siberian

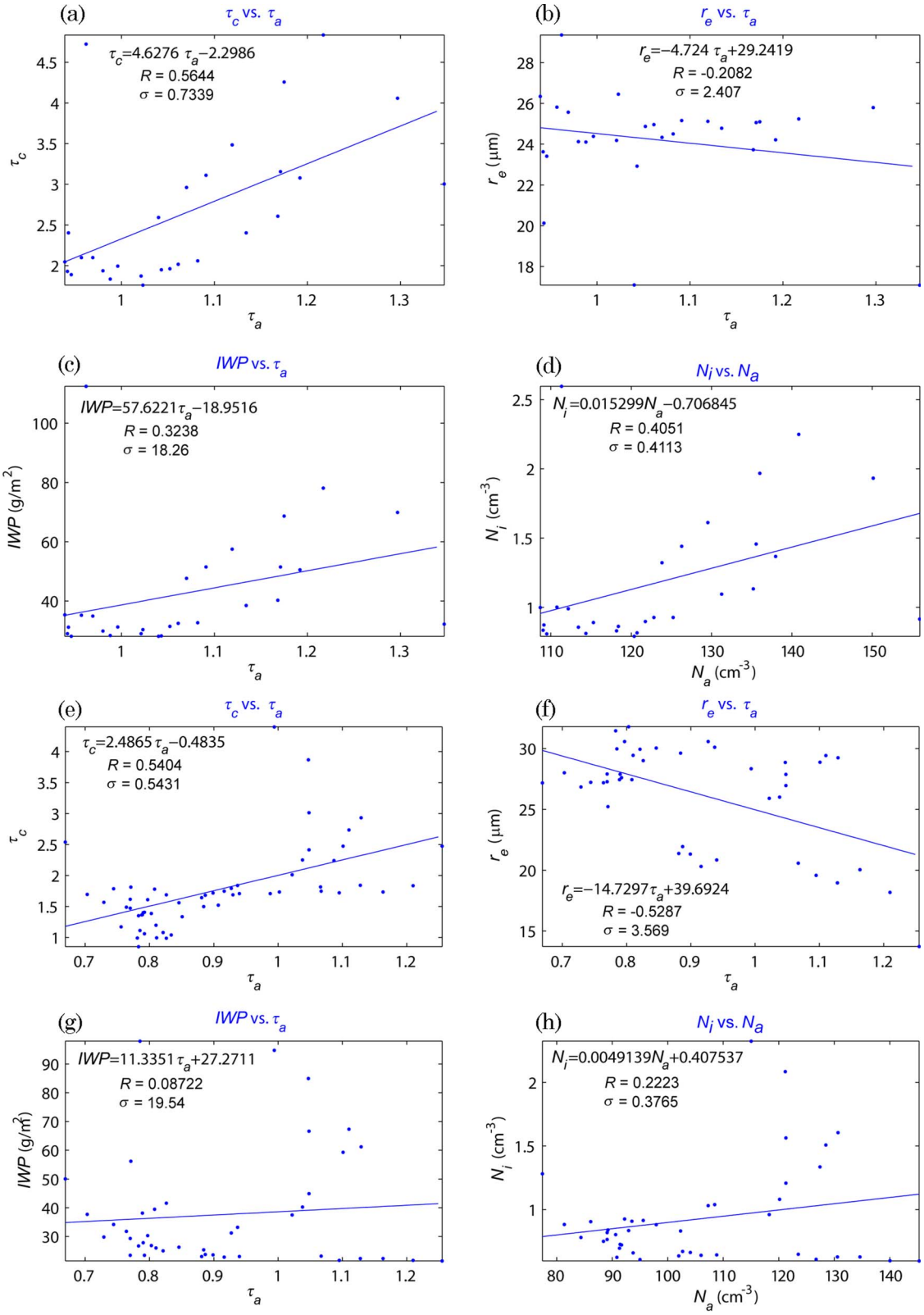

Fig. 4. (Color online) (a)–(d) Same as Figs. 2(e)–2(h), except for domain A of MODIS scene over Korea and Japan for the date 20 March 2001 at 0255 UTC. (e)–(h) Same as Figs. 2(e)–2(h), except for domain *B*.

coast. This band is presumably the remnant of a northern China dust outbreak transported across the northwest Pacific Ocean. Near the northeast corner of the scene, we observe an area of transported dust layer characterized by a light-yellowish color background with clouds imbedded in it. Following

the same approach as above, we selected regions A and B, which contain cirrus clouds on top of the dust layers of different loading. Within these regions, BTD11-12 and BTD8-11 vary between 0 and 2 K and between 0 and 5 K, respectively, and indicate semitransparent to opaque cirrus clouds. Also, the 1.38 μm band reflectance and cloud-phase mask both indicate that these two regions contain patchy opaque ice clouds. Table 2 gives a list of parameters and their mean values for the two regions. For region A, τ_a and r_e vary between 0.9 and 1.3 [Fig. 3(e)] and 5 and 45 μm [Fig. 3(f)], with mean values of 1.07 and 20.3 μm, respectively. For region B, τ_a and r_e vary between 0.7 and 1.2 [Fig. 3(e)] and 16 and 45 μm [Fig. 3(f)], with mean values of 0.88 and 27.8 μm, respectively. This case again convincingly demonstrates the Twomey effect for dust–ice cloud interactions, i.e., larger dust optical depths are coupled with smaller ice particle sizes.

A number of correlation studies have been carried out: cirrus and dust optical depths (τ_c and τ_a), cirrus particle size and dust optical depth (r_e and τ_a), ice water path and dust optical depth (IWP and τ_a), and number concentrations for ice and dust (N_i and N_a). Figures 4(a)–4(d) display the resulting correlation plots along with R and σ for domain A. The majority of sampled optical depths for cirrus are between 1.5 and 5 with particle sizes from 20 to 30 μm. IWP values are within 30 and 80 g m^{-2}. The number concentration N_i varies between 0.8 and 2.5 cm^{-3} and N_a between 11 and 16 cm^{-3}. Figures 4(e)–4(h) show the same correlation plots along with R and σ for domain B. In this case, the cirrus optical depths are between 0.9 and 4, with particle sizes ranging from 14 to 32 μm. The range of IWP covers 20–90 g m^{-2}. The number concentrations N_i and N_a vary between 0.5–2.5 cm^{-3} and 8–15 cm^{-3}, respectively. As in Figs. 2(e)–2(h), linear fittings of data points illustrate that cirrus optical depth and IWP generally increases with aerosol optical depth, while mean effective ice particle size decreases with increasing dust optical depth. Moreover, cirrus cloud number concentration increases with dust number concentration.

In particular for region B, based on the mean retrieved ice particle effective size r_e and the mean dust optical depth τ_a, as given in Table 2, and the slope $\Delta r_e/\Delta\tau_a = -14.73\,\mu$m as shown in Fig. 4(f), we obtained an AIE index of 0.46, which is about 2/3 of the value derived from Fig. 2(f), pointing to a weaker Twomey effect. However, R is larger in magnitude (–0.53), while σ is smaller (3.6 μm), indicating a better correlation, because clouds are more homogeneous, as indicated by a smaller range of variation in $\tau_c (1 < \tau_c < 4)$, than that displayed in Fig. 2(f). These comparisons suffice to demonstrate that the Twomey effect cannot be related to R and σ.

Table 2. Parameter Ranges and Their Mean Values for Domains A and B of the MODIS Scene for 20 March 2001 at 0255 UTC over Korea and Japan

	Parameter Range (mean value)			
Region	τ_c	r_e (μm)	$T_c(K)$	τ_a
A	0–100 (9.8)	5–45(20.3)	215–250(230)	0.9–1.3(1.07)
B	0–10(3.8)	16–45(27.8)	220–250(225)	0.7–1.2(0.88)

4. Concluding Remarks

This study addresses the aerosol indirect effect of the first kind on ice cloud formation by analyzing pertinent data from Terra/Aqua/MODIS. Our analysis focused on the examination of variability in the correlation between ice cloud parameters and tropospheric dust parameters inferred from the available satellite cloud and aerosol data results. We selected and collected suitable aerosol/ice-cloud scenes, identified analysis regions, statistically correlated ice cloud and aerosol parameters, and interpreted resulting correlation trends based on physical principles.

We demonstrated that the dust indirect effect on cirrus clouds can be detected and reasonably quantified by satellite observations. For the CRYSTAL-FACE case (29 July 2002), with the support of ground-based lidar observation, we identified a region of ice clouds formed on top of a transported African dust layer. Satellite derived ice cloud and dust properties were shown to agree reasonably with *in situ* and ground-based measurements. Correlations of ice cloud and dust properties indicate strong aerosol indirect effect existed within this region. For the Eastern Atlantic Ocean case (23 September 2006) and the Korea case (20 March 2001), we identified a number of relevant cirrus cloud regions with different dust loadings. By means of the MODIS retrieved cirrus mean effective sizes and aerosol optical depths, we demonstrated that there is a negative correlation between these two parameters. Correlations between ice cloud and dust properties for the Korean case display the same trends as the CRYSTAL-FACE case. The preceding demonstrative results provide new evidence of dust and ice cloud interactions that are in consistent with the hypothesis of the Twomey effect for water clouds.

The research of this work has been supported by U.S. Air Force Office of Scientific Research (AFOSR) grant FA9550-07-1-0408 and NASA grant NNX08AN69G.

References

1. K. N. Liou, S. C. Ou, and G. Koenig, "An investigation on the climatic effect of contrail cirrus," in *Air Traffic and the Environment Background, Tendencies and Potential Global Atmospheric Effects*, U. Schumann, ed., Lecture Notes in Engineering (Springer-Verlag, 1990), pp. 154–169.
2. D. Frankel, K. N. Liou, S. C. Ou, D. P. Wylie, and P. Menzel, "Observations of cirrus cloud extent and their impacts to climate,," in *Proceedings for the Ninth Conference on Atmospheric Radiation* (American Meteorological Society, 1997), pp. 414–417.

3. D. Wylie, D. L. Jackson, W. P. Menzel, and J. J. Bates, "Trends in global cloud cover in two decades of HIRS observations," J. Climate **18**, 3021–3031 (2005).
4. S. C. Ou and K. N. Liou, "Contrail/cirrus optics and radiation," a subject specific white paper written under the support of the Federal Aviation Agency's Aviation-Climate Change Research Initiative (ACCRI) Project (2008), p. 77.
5. P. Forster, V. Ramaswamy, and P. Artaxo, "Changes in atmospheric constituents and in radiative forcing," in *Climate Change 2007: The Physical Science Basis. Contribution of Working Group I to the Fourth Assessment Report of the Intergovernmental Panel on Climate Change*, S. Solomon, ed. (Cambridge University Press, 2007).
6. P. Minnis, U. Schumann, D. R. Doelling, K. Gierens, and D. Fahey, "Global distribution of contrail radiative forcing," Geophys. Res. Lett. **26**, 1853–1856 (1999).
7. U. Lohmann and J. Feichter, "Global indirect aerosol effects: a review," Atmos. Chem. Phys. **5**, 715–737 (2005).
8. S. Twomey, "The influence of pollution on the shortwave albedo of clouds," J. Atmos. Sci. **34**, 1149–1152 (1977).
9. K. N. Liou and S. C. Ou, "The role of cloud microphysical processes in climate: an assessment from a one-dimensional perspective," J. Geophys. Res. **94**, 8599–8607 (1989).
10. B. A. Albrecht, "Aerosols, cloud microphysics, and fractional cloudiness," Science **245**, 1227–1230 (1989).
11. H. Grassl, "Possible changes of planetary albedo due to aerosol particles," in *Man's Impact on Climate*, W. Bach, J. Pankrath, and W. Kellogg, eds. (Elsevier, 1979).
12. J. Hansen, M. Sato, and R. Ruedy, "Radiative forcing and climate response," J. Geophys. Res. **102**, 6831–6864 (1997).
13. J. A. Coakley Jr., J. R. Bernstein, and P. A. Durkee, "Effect of ship track effluents on cloud reflectivity," Science **237**, 1020–1021 (1987).
14. Y. J. Kaufman, I. Koren, L. A. Remer, D. Rosenfeld, and Y. Rudich, "The effect of smoke, dust, and pollution aerosol on shallow cloud development over the Atlantic Ocean," Proc. Natl. Acad. Sci. USA **102**, 11207–11212 (2005).
15. W. Cantrell and A. Heymsfield, "Production of ice in tropospheric clouds: a review," Bull. Am. Meteorol. Soc. **86**, 795–807 (2005).
16. Y. S. Chung and M. A. Yoon, "On the occurrence of yellow sand and atmospheric loadings," Atmos. Environ. **30**, 2387–2397 (1996).
17. I. Chiapello, J. M. Prospero, J. R. Herman, and N. C. Hsu, "Detection of mineral dust over the North Atlantic Ocean and Africa with the Nimbus 7 TOMS," J. Geophys. Res. **104**, 9277–9291 (1999).
18. J. M. Prospero, "Long-term measurements of the transport of African mineral dust to the southeastern United States: implications for regional air quality," J. Geophys. Res. **104**, 15917–15927 (1999).
19. K. Sassen, P. J. DeMott, J. M. Prospero, and M. R. Poellot, "Saharan dust storms and indirect aerosol effects on clouds: CRYSTAL-FACE results," Geophys. Res. Lett. **30**, 35-1–35-4 (2003).
20. C. M. Archuleta, P. J. DeMott, and S. M. Kreidenweis, "Ice nucleation by surrogates for atmospheric mineral dust and mineral dust/sulfate particles at cirrus temperatures," Atmos. Chem. Phys. **5**, 2617–2634 (2005).
21. L. A. Remer, D. Tanré, and Y. J. Kaufman, "Algorithm for remote sensing of tropospheric aerosol from MODIS: Collection 005," MODIS Algorithm Theoretical Basis Document ATBD-MOD-04 (NASA Goddard Space Flight Center, 2006), available at http://modis-atmos.gsfc.nasa.gov/_docs/ MOD04: MYD04_ATBD_C005_rev1.pdf.
22. K. N. Liou, *An Introduction to Atmospheric Radiation*, 2nd ed. (Academic, 2002), p. 583.
23. C. M. R. Platt, J. C. Scott, and A. C. Dilley, "Remote sounding of high clouds. Part IV: Optical properties of mid-latitude and tropical cirrus," J. Atmos. Sci. **44**, 729–747 (1987).
24. A. J. Heymsfield, C. Schmitt, A. Bansemer, G.-J. van Zadelhoff, M. J. McGill, C. Twohy, and D. Baumgardner, "Effective radius of ice particle populations derived from aircraft probes," J. Atmos. Oceanic Technol. **23**, 361–380 (2006).
25. I. N. Sokolik and O. B. Toon, "Incorporation of mineralogical composition into models of the radiative properties of mineral aerosol from UV to IR wavelengths," J. Geophys. Res. **104**, 9423–9444 (1999).
26. G. A. d'Almeida, P. Koepke, and E. P. Shettle, *Atmospheric Aerosols, Global Climatology and Radiative Characteristics* (A. Deepak Publishing, 1991), p. 561.
27. Y. J. Kaufman, L. A. Remer, D. Tanré, R.-R. Li, R. Kleidman, S. Mattoo, R. C. Levy, T. F. Eck, B. N. Holben, C. Ichoku, J. V. Martins, and I. Koren, "A critical examination of the residual cloud contamination and diurnal sampling effects on MODIS estimates of aerosol over ocean," IEEE Trans. Geosci. Remote Sensing **43**, 2886–2897 (2005).
28. B.-C. Gao, Y. J. Kaufman, D. Tanre, and R.-.R. Li, "Distinguishing tropospheric aerosols from thin cirrus clouds for improved aerosol retrievals using the ratio of 1.38 μm and 1.24 μm channels," Geophys. Res. Lett. **29**, 1890–1892 (2002).
29. Y. Takano and K. N. Liou, "Solar radiative transfer in cirrus clouds. Part I: Single-scattering and optical properties of hexagonal ice crystals," J. Atmos. Sci. **46**, 3–19 (1989).
30. P. Yang and K. N. Liou, "Light scattering by hexagonal ice crystals: comparison of finite difference time domain and geometric optics models," J. Opt. Soc. Am. A **12**, 162–176 (1995).
31. M. D. King, S.-C. Tsay, S. E. Platnick, M. Wang, and K. N. Liou, "Cloud retrieval algorithms for MODIS: optical thickness, effective particle radius, and thermodynamic phase," MODIS Algorithm Theoretical Basis Document ATBDMOD-05 (NASA Goddard Space Flight Center, 1997), version 5, available at http://modis-atmos.gsfc.nasa.gov/_docs/atbd_mod05.pdf.
32. P. J. DeMott, K. Sassen, M. R. Poellot, D. Baumgardner, D. C. Rogers, S. Brooks, A. J. Prenni, and S. M. Kreidenweis, "African dust aerosols as atmospheric ice nuclei," Geophys. Res. Lett. **30**, ASC 1-1–1-4 (2003).
33. G. Feingold, W. L. Eberhard, D. E. Veron, and M. Previdi, "First measurements of the Twomey indirect effect using ground-based remote sensors," Geophys. Res. Lett. **30**, 1287–1289 (2003).